PAPER

Broadband light confinement using a hierarchically structured TiO$_2$ multi-layer for dye-sensitized solar cells†

Yong-June Chang,[a] Eui-Hyun Kong,[a] Yoon-Cheol Park[b] and Hyun Myung Jang*[a]

Herein, we present a simple strategy for broadband light confinement without sacrificing dye-loading capacity by suitably combining multi-layer architecture with hierarchically structured TiO$_2$. For this purpose, three distinct TiO$_2$ hierarchical nanomaterials were exploited to simultaneously realize high internal surface area and a graded series of optical properties (in terms of reflectance and transmittance). The present hierarchically structured multi-layer showed a remarkable improvement in the overall efficiency for dye-sensitized solar cells (DSCs): a maximum of 11.43% at 1 Sun (12.16% at 1/8 Sun) *versus* 8.15% at 1 Sun (8.26% at 1/8 Sun) for the reference cell made of a nanocrystalline TiO$_2$ single-layer. This notable result is attributed to the synergetic effects of the enhanced broadband light confinement, dye-loading, and charge-collection efficiency.

1 Introduction

Solar power has received much attention these days with a growing demand for sustainable and renewable energy sources.[1] In the past two decades, dye-sensitized solar cells (DSCs) have emerged as a promising alternative to the expensive silicon-based devices because of their low-cost and high efficiency.[2,3] To date, a tremendous amount of research has been focused on the morphological properties of the oxide photoelectrodes to improve the performance of DSCs.[4] It is widely known that ~20 nm-sized anatase TiO$_2$ is most effective for optimal dye-loading in the working electrodes.[5] However, TiO$_2$ nanoparticles alone are not preferred to be used as the photoelectrode because of their high transparency and weak light scattering in the visible range. This may result in a significant loss of the incident light, thereby limiting the photocurrent generation in DSCs. Thus, efficient light scattering has become one of the major concerns in designing photoelectrodes.[6–8]

From a structural viewpoint, various architectures were proposed to achieve strong photon confinement in DSCs:[9] (i) single TiO$_2$ layers containing light scatterers (sub-micron beads, spherical voids, or other nanostructures),[10–13] (ii) bi-layers made of a nanocrystalline TiO$_2$ film and a light-scattering layer (usually comprised of large TiO$_2$ particles),[14–16] and (iii) a multi-layer structure with gradually increasing haziness.[17,18] Among

these strategies, multi-layer is considered to be an ideal configuration for efficient light confinement over a broad wavelength range. However, their structural complexity may require a state-of-the-art technique to balance the two opposing factors: light scattering effect and dye-loading capacity.[17]

On the materials engineering side, the oxide hierarchical nano-structures have made recent progress as competitive building blocks in DSCs.[19] These nanostructures consist of tiny nanocrystallites that are aggregated to form large sub-micrometer-sized spheres. Their structural nature enables them to have similar or even higher internal surface area, as compared with a conventional nanocrystalline film. Therefore, they function as light scatterers without the loss of dye-uptake.[20] Although these purpose-built nanomaterials have been suggested as single-layers[21–24] or over-layers[25–30] on the nanocrystalline TiO$_2$ films (for bi-layers), little attention has been paid to applications in multi-layered photoelectrodes in DSCs.

Herein, we present a new strategy that can simultaneously satisfy broadband light confinement and high dye-loading capacity by suitably combining the optically tunable multi-layer architecture with the hierarchically structured TiO$_2$. For this, we prepared three distinct TiO$_2$ layers with a graded series of optical properties (Fig. 1a) by tailoring the degree of the hierarchical order. On the other hand, Fig. 1b presents a schematic diagram of three types of hierarchical materials in terms of the microstructure. Each type has a different degree of hierarchical order owing to the network of primary particles. Type I corresponds to typical mesoporous nanoparticles. Since TiO$_2$ nanocrystallites are randomly distributed, a secondary structure does not exist in this configuration (zero order in the hierarchy). In contrast, type II and type III particles have a certain degree of hierarchical order. In type II, a spherical assembly of loose aggregation is observed. Meanwhile, tiny nanograins are tightly

[a]*Department of Materials Science and Engineering, and Division of Advanced Materials Science, Pohang University of Science and Technology (POSTECH), Pohang 790-784, Korea. E-mail: hmjang@postech.ac.kr*

[b]*Research Institute of Industrial Science and Technology (RIST), Pohang 790-784, Korea*

† Electronic supplementary information (ESI) available: Light confinement effect and the dye-loading capacity of type I, II, and III films. See DOI: 10.1039/c3ta11527e

bound to each other to create large spherical particles in type III (see the "Results and discussion" section for details).

2 Experimental

Materials

The chemicals used in the synthesis of the hierarchically structured TiO_2 were titanium(IV) tetraethoxide (TTE, technical grade, Sigma-Aldrich), sodium chloride (NaCl, 99.5%, Kanto Chem.), hexadecylamine (HDA, 90%, Sigma-Aldrich), absolute ethanol (99.9%, J. T. Baker), deionized water (18.0 MΩ cm), and N719 dye (Solaronix). To prepare the electrolyte, acetonitrile (99.5%, Aldrich), valeronitrile (99.5%, Aldrich), iodine (I_2, 99.99%, Aldrich), 1-butyl-3-methylimidazolium iodide (BMII, 95%, Tokyo Chem. Ind.), guanidinium thiocyanate (GSCN, 97%, Sigma-Aldrich), and 4-tert-butylpyridine (TBP, 99%, Aldrich) were used. For type I, 20 nm-sized commercial TiO_2 nanoparticle paste was purchased from ENB Korea.

Synthesis of the hierarchically structured TiO_2 particles [type II and type III]

Type II and type III particles (Fig. 1b) were synthesized via a two-step process: (a) dilute-mixing-driven hydrolysis of titanium(IV) tetraethoxide (TTE) and (b) solvothermal reaction.[27,31,32] As a first step, two separate solutions were prepared: (1) 4.28 g of TTE in 125 mL of ethanol, (2) 1.575 g of 0.1 M NaCl aqueous solution and 1.66 g of HDA in 125 mL of ethanol. Solution (1) was added into solution (2) under stirring at room temperature. The resulting colloidal dispersion was kept undisturbed for 2 h at ambient temperature, and submicrometer-sized amorphous TiO_2 beads were then obtained. It was reported that the bead size can be controlled along with the [water]/[TTE] ratio.[27] In the present study, the aforementioned chemical composition was chosen, for the reason that the most reflective feature was required in the as-synthesized particles. TiO_2 precipitates were then washed thoroughly by repeated centrifugation (2000 rpm) and sonication. After that, they were dispersed in a mixed solution of 96 mL ethanol and 48 mL deionized water. As a subsequent step, the mixture was sealed in a solvothermal reactor and heated at 160 °C for 16 h. Consequently, the anatase TiO_2 hierarchical particles were obtained, having a diameter of 587 nm (type III). In order to prepare type II, chemically and mechanically assisted treatments were performed: solvothermal reaction under a basic environment, and subsequent ball milling. For this, 6 mL of ammonia was used during the solvothermal process, and then the resulting precipitates underwent ball milling with 5 mm-sized ZrO_2 balls for 1 h. Finally, around 600 nm-sized TiO_2 particles with a low degree of hierarchical order were prepared (type II).

Fabrication of the DSCs

The devices were fabricated as described in the previous literature with some modifications.[15,27] Three types of the hierarchically structured TiO_2 were cast on the F-doped SnO_2 (FTO) substrates. ~7 μm-thick type I was deposited as an under-layer, then type II and III particles were printed as over-layers with the same thickness to construct a ~21 μm-thick hierarchically

structured multi-layer (HSM). The HSM was compared to a nanocrystalline TiO_2 single-layer (NC). The as-prepared working electrodes were heat-treated with the following temperature profile: (i) 325 °C for 5 min, (ii) 375 °C for 5 min, (iii) 450 °C for 15 min, and (iv) 500 °C for 15 min. The electrodes were processed with a 40 mM $TiCl_4$ aqueous solution at 70 °C for 30 min, which was followed by thermal treatment at 500 °C for 30 min. Then, they were immersed into a 0.3 mM N719 dye solution for 12 h at room temperature. A thermally platinized FTO glass (Platisol, Solaronix) was used as a counter electrode. For the cell assembly, a 60 μm-thick Surlyn (Meltonix 1170-60, Solaronix) sheet was used to separate the photoanode and the counter electrode. The edge of each electrode was treated with a solder to obtain a good electrical contact. As an electrolyte, 0.03 M I_2, 0.7 M BMII, 0.5 M TBP, and 0.1 M GSCN were blended and dissolved in acetonitrile–valeronitrile (85/15, v/v).

Characterization

The morphology of three hierarchically structured TiO_2 samples was studied using a field-emission scanning electron microscope (FE-SEM; JEOL, JSM-7401). SEM images were taken under high vacuum without platinum coating on the samples. To observe detailed nanostructures, a high-resolution transmission electron microscope (HR-TEM; JEOL, JEM-2200FS) in NCNT (National Center for Nanomaterials Technology in Pohang) was used. X-ray diffraction (XRD; Rigaku, RINT 2000 with Cu Kα ray) was utilized to investigate the crystal structure and crystallite size of each sample. The nitrogen-sorption measurement was carried out using a Micromeritics ASAP 2010 system. Diffuse reflectance, transmittance, and absorbance spectra were recorded using a PerkinElmer UV-Vis spectrometer Lambda 750S.

The photovoltaic performance was evaluated under the illumination of a solar simulator (Newport, 92251A; under AM1.5, 1 Sun & 1/8 Sun). The incident-photon-to-current conversion efficiency (IPCE) values at a chopping frequency of 4 Hz were recorded as a function of the wavelength from 400 nm to 800 nm (PV Measurements, Inc). A 75 W xenon lamp was used as a light source with a monochromator. The intensity-modulated photocurrent/photovoltage spectroscopy (IMPS/IMVS) measurements were conducted on the electrochemical work station (Zahner, Zennium) with a frequency response analyzer under the irradiation of a 625 nm light emitting diode, which was driven by a source supply (Zahner, RTL01). The modulated light intensity was set to be 10% of the basic light intensity, and the frequency range was 10^{-2} to 10^2 Hz. The incident light intensity was controlled from 10 to 150 mW cm^{-2}. For the evaluation of the dye-loading capacity, N719 dye molecules chemisorbed on the TiO_2 surface were dissolved in a 0.1 M NaOH solution (water–ethanol, 50/50, v/v), and their absorbance values were subsequently analyzed using a UV-Vis spectrometer (PerkinElmer, Lambda 750S).

3 Results and discussion

Three types of hierarchically structured TiO_2 particles

As presented in Fig. 1b, we have classified three groups of the hierarchical structures in terms of optical properties. Type I is a
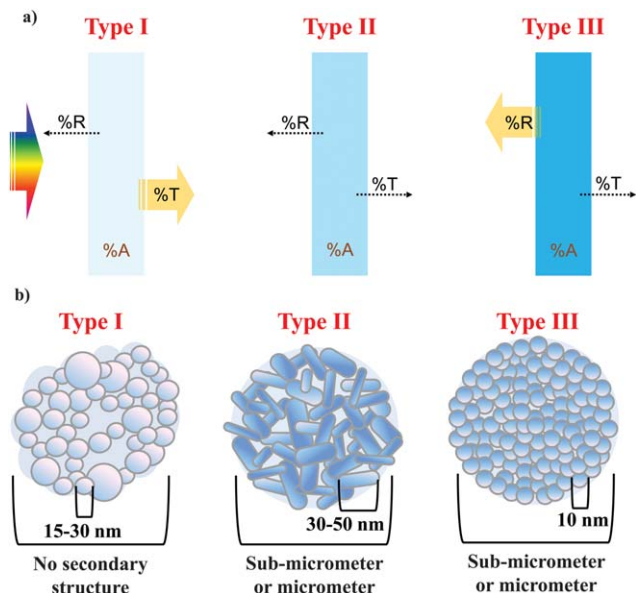
9708 | J. Mater. Chem. A, 2013, **1**, 9707–9713

This journal is © The Royal Society of Chemistry 2013

Fig. 1 A classification of the three hierarchically structured TiO$_2$ nanomaterials (type I, II, and III) in terms of (a) the optical properties and (b) the microstructure.

Fig. 2 SEM images of (a) type I, (b) type II, and (c) type III. Each inset shows the same image with lower magnification. (d–f) The corresponding TEM images of the primary particles for each sample.

typical nanoparticle film, which shows relatively low reflectance and high transmittance. In contrast, type III has opposing optical characters: high reflectance and low transmittance. Various nanostructures that are micrometers or sub-micrometers in size can be categorized in this configuration. One can imagine an intermediate state of the nanomaterial between type I and type III (called type II). This type of film may show reduced values both in reflectance and transmittance over a wide wavelength range. Therefore, it is reasonable to expect that simply layering these three films can promote red-light harvesting *via* the gradually increasing light-scattering effect inside the photoanode.

For type I, optically translucent TiO$_2$ nanoparticles were chosen. Type II and III particles were prepared through a two-step process: dilute-mixing-assisted hydrolysis of titanium(IV) tetraethoxide (TTE) and solvothermal reaction. In hydrolysis, water concentration plays an essential role in controlling the diameter of amorphous TiO$_2$ spheres. The resulting particle size is maintained even after the solvothermal reaction (587–1554 nm), and governs their scattering efficiencies.[27] In this paper, the most reflective hierarchical nanomaterials (587 nm) are used for type III. On the other hand, the subsequent process may affect the hierarchical order.[27,31,32] Indeed, the addition of ammonia during the solvothermal treatment gives rise to the morphological change of the primary particles, producing ∼600 nm-sized mesoporous spherical TiO$_2$ with a low degree of the hierarchical order. This was used as type II.

Microscopic images of the three hierarchically structured TiO$_2$ samples (types I, II, and III) are presented in Fig. 2. A high magnification FE-SEM image reveals the polydisperse feature of type I particles that are about 15–30 nm in size, and the inset indicates that there is no hierarchical order (Fig. 2a). The HR-TEM image shows that type I is fully crystalline with the lattice spacing of 0.352 nm (Fig. 2d). This corresponds to the anatase
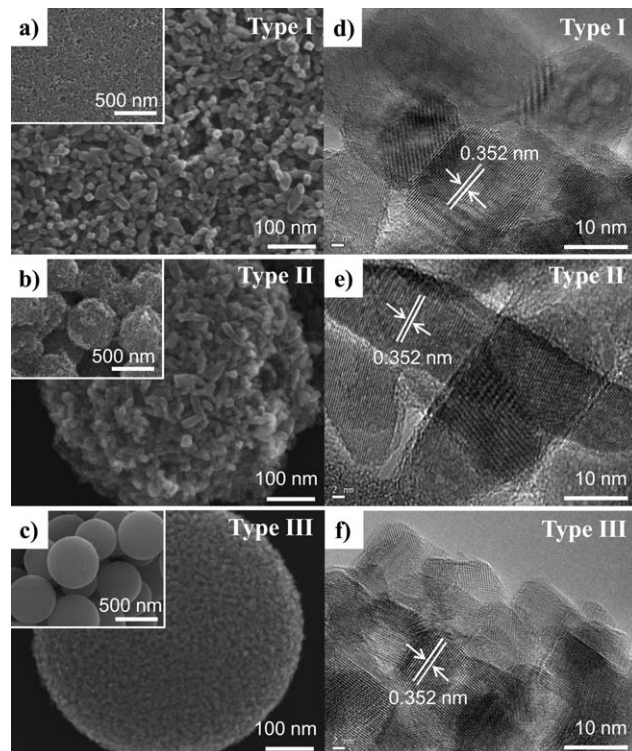
(101) plane. It is observed in Fig. 2b that needle-like polydisperse nanocrystallites, having a mean diameter of around 15 nm and a length of about 30–50 nm, seem to be loosely agglomerated, and build a submicrometer-sized sphere. The corresponding HR-TEM image provides the crystal structure of type II, where the same inter-lattice distance of 0.352 nm can be seen, implying that the anatase (101) facets are dominant in type II (Fig. 2e). On the other hand, tiny primary particles are densely aggregated inside the type III sphere (Fig. 2c). Fig. 2f presents a HR-TEM image of type III, indicating that the primary crystallites are ∼10 nm in diameter, and their size distribution is fairly monodisperse.

The XRD patterns (Fig. 3) show that all three types of hierarchical nanomaterials are in the anatase phase after calcination, in good agreement with the previous HR-TEM result (Fig. 2). The crystalline size of each sample was estimated from the full-width at half maximum (FWHM) of the anatase (101) peak using the Scherrer equation. The diameters of the primary particles for types I, II, and III are 17.61 nm, 14.79 nm, and 8.53 nm, respectively.

The surface area and the pore-size distribution were examined by the nitrogen-sorption analysis (Fig. 4). The physical properties of the three types of particles are summarized in Table 1. The specific surface area of the three samples was calculated by employing the Brunauer–Emmett–Teller (BET) adsorption model. It was confirmed that each sample possesses a sufficient internal surface area larger than ∼70 m^2 g^{-1}. For all three particles, H1 type hysteresis and type IV isotherms with a
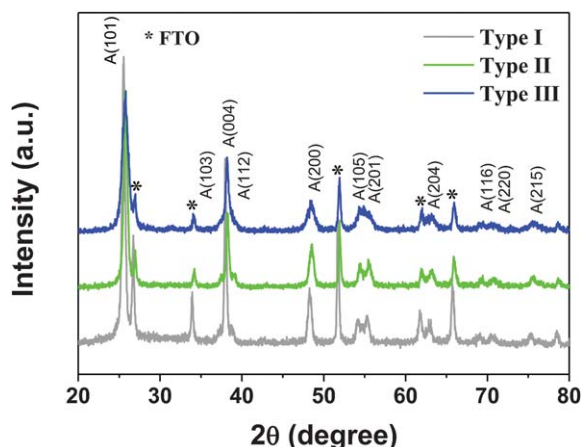
Fig. 3 XRD patterns of type I, II, and III samples after calcination at 500 °C for 30 min.
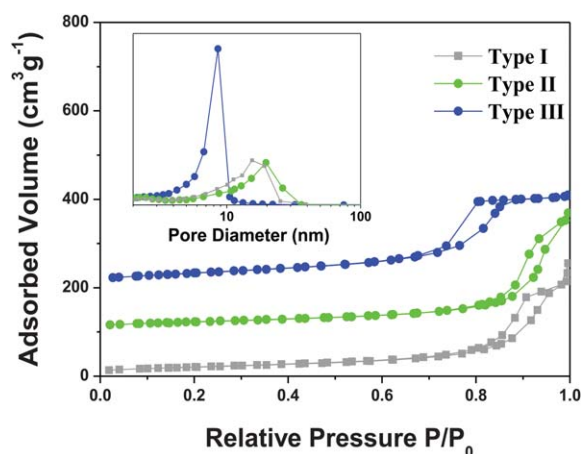

Fig. 4 Nitrogen-sorption isotherms of type I, II, and III particles after calcination at 500 °C for 30 min. For the sake of clear presentation, the isotherms of types II and III are vertically shifted by 100 and 200 cm^3 g^{-1}, respectively. The inset shows the corresponding pore-size distribution, estimated using the BJH model.

sharp capillary-condensation step are commonly observed at high relative pressures ($P/P_0 = 0.8$–0.9), which supports the presence of the meso-scale pore structures inside each sample. Type III shows the smallest pore size of 8.9 nm with a narrow size distribution. In contrast, types I and II were calculated to possess enlarged pores (16.4 nm, 17.3 nm, respectively) with a broad pore-size distribution according to the Barrett–Joyner–

Table 1 Physical properties of the three types of hierarchically structured TiO$_2$ determined from nitrogen-gas sorption and XRD analysis

Sample	Surface area (m^2 g^{-1})	Pore size (nm)	$d_{xrd(101)}$[a] (nm)	Diameter of spheres[b] (nm)
Type I	72.5	16.4	17.6	—
Type II	81.6	17.3	14.8	∼600
Type III	93.7	8.9	8.5	587

[a] The crystallite size was calculated by applying the Scherrer equation to the FWHM of the anatase (101) peak. [b] The mean diameter of the TiO$_2$ particles was obtained from the corresponding SEM image.
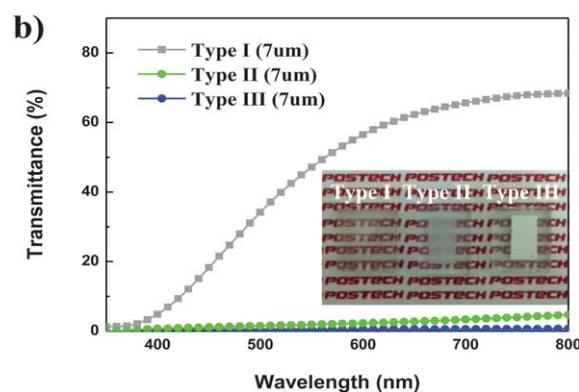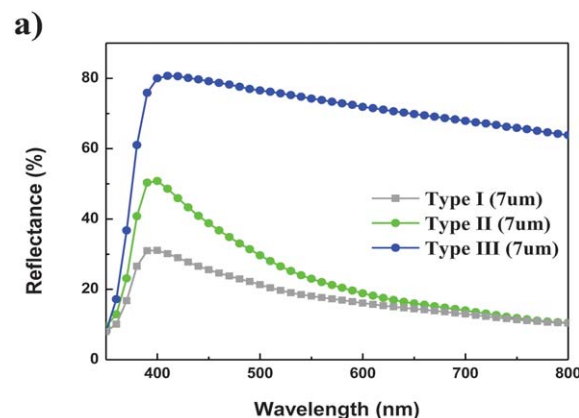

Fig. 5 (a) Diffuse reflectance and (b) transmittance spectra of type I, II, and III films (7 μm). The inset compares the top-view images of films with three different types.

Halenda (BJH) model. This result stems from the morphological diversity in the primary level and a lower degree of hierarchical order in types I and II.

The optical properties were characterized in terms of diffuse reflectance (Fig. 5a) and transmittance (Fig. 5b) of ∼7 μm-thick films with three different types. Since tiny nanocrystallites are closely packed within type III, the aggregate size seemingly dominates the overall optical properties. It is widely known that the light scattering phenomena can be understood by the Mie theory. This implies that there is a specific size for the optimized diffuse reflection capacity over a given spectral range.[33] In type II, the size effect of the secondary structures is weakened as the degree of their aggregation becomes looser. Type I consists of randomly oriented nanoparticles with no order in the hierarchy, thereby causing the secondary-particle size effect on light scattering to vanish. Consequently, the type III film showed the highest reflectance among the three types of films while type II and type I showed much reduced reflectance values over a broad wavelength range. However, the three hierarchically structured films show different aspects in the transmittance spectra. The least reflective type I film performed the highest transmittance, and the type II and type III films ranked behind type I with essentially negligible values. Since the type II particle possesses a lower hierarchical order than type III, a slight degree of transmittance was still observed, as shown in the inset of Fig. 5b.

Enhanced light confinement and overall efficiency

To construct a multi-layer structure, approximately 7 μm-thick films made of type I, II, and III particles were screen-printed on the translucent FTO glass (Fig. 6). This hierarchically structured multi-layer (HSM) was compared with the reference nano-crystalline TiO$_2$ single-layer (NC). The light-confinement effect was characterized by measuring the absorbance spectra of the two distinct photoelectrodes after sensitization with the N719 dye (Fig. 7). Since TiO$_2$ nanocrystallites are weak scatterers in the visible range of light, a significant portion of the incident light can pass through the NC film, resulting in a huge optical loss especially over the long wavelength range (600–800 nm). In contrast, the sensitized HSM film exhibits considerably high absorbance over a broad spectral range. This indicates that the sensitized HSM film is much superior in light confinement in comparison with the reference NC.
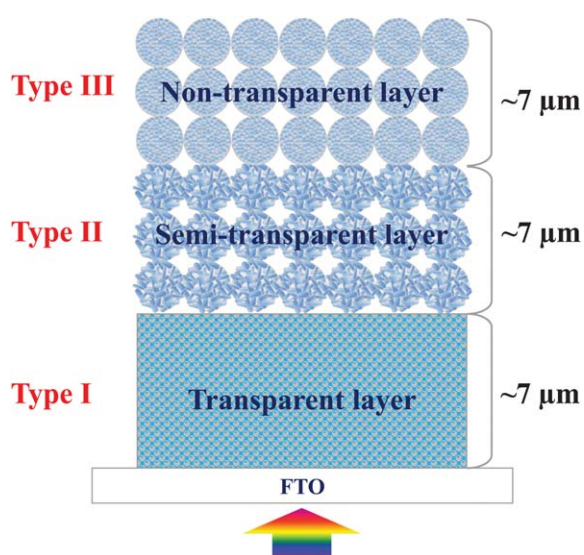

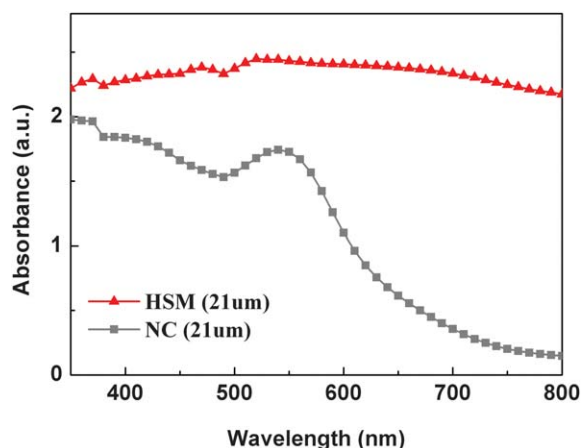**Fig. 6** A schematic of the hierarchically structured multi-layer (HSM).

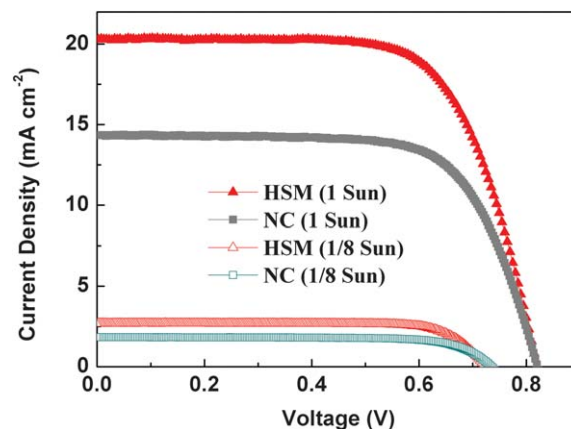**Fig. 7** Absorbance spectra of the HSM and the NC photoelectrodes after sensitization with N719.

Fig. 8 I–V curves of the HSM- and the NC-DSCs under illumination of 1 Sun and 1/8 Sun.

I–V curves of the HSM- and the NC-DSCs are shown in Fig. 8. In Table 2, the photovoltaic properties of the two devices are listed. The NC-device showed the overall efficiency (η) of 8.15% with a photocurrent density (J_{sc}) of 14.3 mA cm^{-2} and an open-circuit voltage (V_{oc}) of 819.6 mV under AM1.5, 1 Sun illumination (η of 8.26% with J_{sc} of 1.9 mA cm^{-2} and V_{oc} of 726.3 mV under 1/8 Sun). By constructing multi-layers, a noticeable improvement is achieved in light harvesting, which is mainly attributed to the increased photocurrent density. The HSM cell demonstrated an η of 11.43% with a J_{sc} of 20.3 mA cm^{-2} and a V_{oc} of 819.6 mV under AM1.5, 1 Sun illumination. Under lower irradiation (1/8 Sun), the cell efficiency (η) increases to 12.16% with a J_{sc} of 2.7 mA cm^{-2} and a V_{oc} of 723.3 mV. Since type II and type III particles possess higher internal surface areas than type I, the combination of the three types of the hierarchical TiO$_2$ offers more space for the dye-uptake, which is quantitatively verified in the dye-loading capacity of two working electrodes: 2.601 × 10^{-7} mol cm^{-2} for the HSM versus 2.461 × 10^{-7} mol cm^{-2} for the NC film. Moreover, the HSM cell is able to more efficiently recapture unabsorbed light via gradually changing optical properties.

The incident-photon-to-current conversion efficiency (IPCE) provides a detailed description of the light-harvesting performance of the HSM- and the NC-DSCs. It is observed in Fig. 9 that the HSM cell exhibits markedly higher IPCE values than the NC cell over the whole spectral range, and the efficiency gap between the two devices becomes more significant over the long

Table 2 Photovoltaic properties (short-circuit current density, open-circuit voltage, fill factor, and overall efficiency) with the dye-loading capacity of the hierarchically structured multi-layer (HSM) and the reference nanocrystalline TiO$_2$ single-layer (NC)

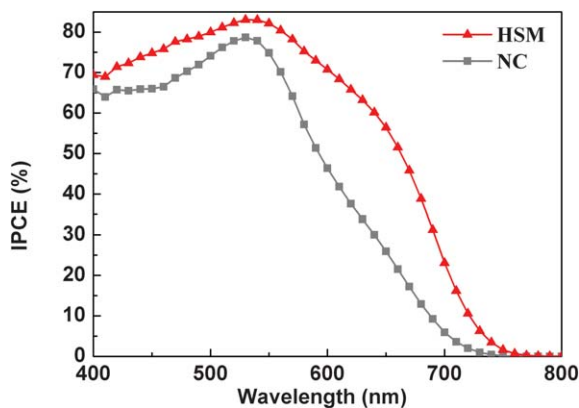| Sample	Illumination (Sun)	J_{sc} (mA cm^{-2})	V_{oc} (mV)	FF (%)	η (%)	Adsorbed dye (10^{-7} mol cm^{-2})
HSM	1	20.3	819.6	68.7	11.43	2.601
HSM	1/8	2.7	723.3	77.8	12.16	2.601
NC	1	14.3	819.6	69.5	8.15	2.461
NC	1/8	1.9	726.3	74.8	8.26	2.461

Fig. 9 IPCE spectra of the HSM- and the NC-DSCs.

wavelength range (600–800 nm). This improvement supports the strong optical scattering in the HSM device. Accordingly, it can be inferred that the dual effect of high dye loading and light confinement has brought about enhanced optical absorption within the photoelectrode.

The intensity-modulated photocurrent/photovoltage spectroscopy (IMPS/IMVS) measurement was then performed to study the charge-collection properties (Fig. 10). It is well known that IMPS records the photocurrent response to the modulated light under the short-circuit condition while IMVS measures the periodic voltage response to the same irradiation but under the open-circuit condition. In brief, IMPS/IMVS analysis provides quantitative information on electron transport and recombination. The electron transport time (τ_t) is determined by the relation $\tau_t = 1/(2\pi f_t)$, where f_t is the characteristic frequency minimum of the IMPS imaginary part. Then, the effective electron diffusion coefficient (D_n) can be estimated using the following expression: $D_n = L^2/(2.35\tau_t)$, where L is the thickness of the photoelectrode. The recombination time (τ_r) is determined by a similar equation, $\tau_r = 1/(2\pi f_r)$, where f_r is the characteristic frequency minimum from the IMVS imaginary component.[34–36]

The D_n values of the HSM- and the NC-DSCs are presented in Fig. 10a under various conditions of the incident light intensity (10–150 mW cm^{-2}). Thus, the electron transport of the HSM cell is more efficient than that of the NC cell, implying that the HSM electrode gives a faster pathway for the electronic motion. It is presumed that well interconnected networks of primary particles within type II and type III seem to promote electron diffusion *via* multi-layered photoelectrodes.[23] The recombination time (τ_r) of the two devices under various values of incident light intensity is presented in Fig. 10b. It is shown that τ_r of the HSM-DSC is longer than that of the NC cell. This indicates that the charge recombination is relatively more suppressed at the HSM electrode–electrolyte interface.

Finally, the charge-collection efficiency (η_{cc}) was calculated by the two characteristic times obtained from the IMPS/IMVS measurement using the following equation:[36] $\eta_{cc} = 1 - (\tau_t/\tau_r)$. As a result, an η_{cc} of 95.3% is demonstrated in the HSM-DSC at
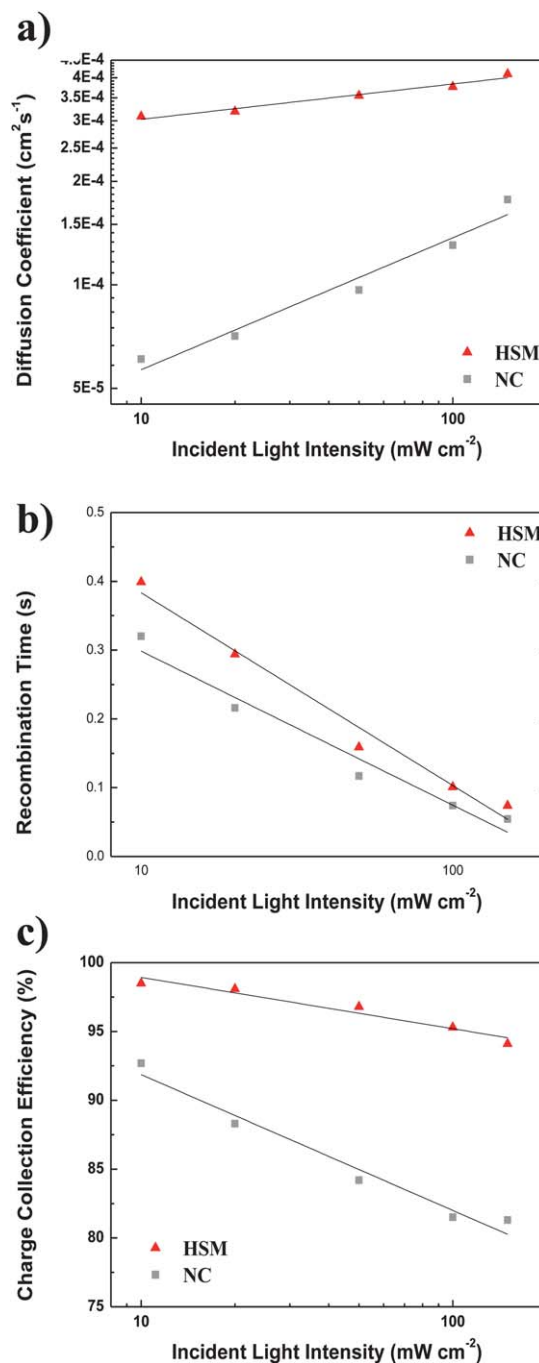

Fig. 10 (a) Incident light dependent effective electron diffusion coefficient, (b) recombination time, and (c) estimated charge-collection efficiency of the HSM- and the NC-DSCs under the irradiation of a 625 nm LED.

100 mW cm^{-2}, while the NC cell shows a limited η_{cc} of 81.5% (Fig. 10c). Therefore, it can be concluded that the HSM cell offers an enhanced charge-collection capability over the NC device. Consequently, it is worth pointing out that the HSM-DSC exhibits superior charge-collection efficiency as well as optical absorption owing to the promotion of both light scattering and dye-loading. This has brought about a synergetic effect for the photocurrent generation, and eventually leads to a remarkable improvement in the overall conversion efficiency.

4 Conclusions

Three types of hierarchical TiO_2 particles were prepared with a graded series of optical properties by controlling the degree of the hierarchical order (types I, II, and III). The hierarchically structured multi-layer (HSM) was demonstrated by layering these three nanomaterials. Since all three layers possess sufficient internal surface area, each layer comprising the HSM cell is able to participate in light harvesting. Therefore, the HSM cell exhibited strong optical absorption *via* light confinement over a broad range of wavelengths without compromising the dye-loading capacity. Moreover, the HSM cell exhibited superior charge-collection efficiency to the reference cell made of a nanocrystalline TiO_2 single-layer (NC). Thus, the synergetic effect of the enhanced optical absorption and charge collection facilitated the photocurrent generation in DSCs (J_{sc} of 20.3 mA cm^{-2} for the HSM *versus* 14.3 mA cm^{-2} for the NC). As a result, 11.43% efficiency was achieved in the HSM-DSC under 1 Sun illumination, which corresponds to ~30% improvement as obtained from the NC. We believe that the present methodology can be extended to various DSCs, and potentially pave a way toward the full utilization of optical absorption.

Notes and references

1 K. Kalyanasundaram and M. Grätzel, *J. Mater. Chem.*, 2012, **22**, 24190–24194.

2 B. O'Regan and M. Grätzel, *Nature*, 1991, **353**, 737–740.

3 M. Grätzel, *Nature*, 2001, **414**, 338–344.

4 N. Tetreault and M. Grätzel, *Energy Environ. Sci.*, 2012, **5**, 8506–8516.

5 J. Ferber and J. Luther, *Sol. Energy Mater. Sol. Cells*, 1998, **54**, 265–275.

6 A. Usami, *Sol. Energy Mater. Sol. Cells*, 2000, **62**, 239–246.

7 A. Usami, *Sol. Energy Mater. Sol. Cells*, 2000, **64**, 73–83.

8 G. Rothenberger, P. Comte and M. Grätzel, *Sol. Energy Mater. Sol. Cells*, 1999, **58**, 321–336.

9 Q. F. Zhang, D. Myers, J. L. Lan, S. A. Jenekhe and G. Z. Cao, *Phys. Chem. Chem. Phys.*, 2012, **14**, 14982–14998.

10 G. T. Yang, J. Zhang, P. Q. Wang, Q. A. Sun, J. Zheng and Y. J. Zhu, *Curr. Appl. Phys.*, 2011, **11**, 376–381.

11 S. Hore, P. Nitz, C. Vetter, C. Prahl, M. Niggemann and R. Kern, *Chem. Commun.*, 2005, 2011–2013.

12 J. H. Yoon, S. R. Jang, R. Vittal, J. Lee and K. J. Kim, *J. Photochem. Photobiol., A*, 2006, **180**, 184–188.

13 Y. Chiba, A. Islam, Y. Watanabe, R. Komiya, N. Koide and L. Y. Han, *Jpn. J. Appl. Phys., Part 2*, 2006, **45**, L638–L640.

14 S. Hore, C. Vetter, R. Kern, H. Smit and A. Hinsch, *Sol. Energy Mater. Sol. Cells*, 2006, **90**, 1176–1188.

15 S. Ito, T. N. Murakami, P. Comte, P. Liska, C. Grätzel, M. K. Nazeeruddin and M. Grätzel, *Thin Solid Films*, 2008, **516**, 4613–4619.

16 S. Ito, M. K. Nazeeruddin, S. M. Zakeeruddin, P. Pechy, P. Comte, M. Grätzel, T. Mizuno, A. Tanaka and T. Koyanagi, *Int. J. Photoenergy*, 2009, 517609.

17 Z. S. Wang, H. Kawauchi, T. Kashima and H. Arakawa, *Coord. Chem. Rev.*, 2004, **248**, 1381–1389.

18 Z. P. Tian, H. M. Tian, X. Y. Wang, S. K. Yuan, J. Y. Zhang, X. B. Zhang, T. Yu and Z. G. Zou, *Appl. Phys. Lett.*, 2009, **94**, 031905.

19 F. Zhu, D. P. Wu, Q. Li, H. Dong, J. M. Li, K. Jiang and D. S. Xu, *RSC Adv.*, 2012, **2**, 11629–11637.

20 T. P. Chou, Q. F. Zhang, G. E. Fryxell and G. Z. Cao, *Adv. Mater.*, 2007, **19**, 2588–2592.

21 D. H. Chen, F. Z. Huang, Y. B. Cheng and R. A. Caruso, *Adv. Mater.*, 2009, **21**, 2206–2210.

22 F. Sauvage, D. H. Chen, P. Comte, F. Z. Huang, L. P. Heiniger, Y. B. Cheng, R. A. Caruso and M. Graetzel, *ACS Nano*, 2010, **4**, 4420–4425.

23 S. R. Gajjela, C. Yap and P. Balaya, *J. Mater. Chem.*, 2012, **22**, 10873–10882.

24 M. Liang, M. Lu, Q. L. Wang, W. Y. Chen, H. Y. Han, Z. Sun and S. Xue, *J. Power Sources*, 2011, **196**, 1657–1664.

25 H. J. Koo, Y. J. Kim, Y. H. Lee, W. I. Lee, K. Kim and N. G. Park, *Adv. Mater.*, 2008, **20**, 195–199.

26 I. G. Yu, Y. J. Kim, H. J. Kim, C. Lee and W. I. Lee, *J. Mater. Chem.*, 2011, **21**, 532–538.

27 Y. C. Park, Y. J. Chang, B. G. Kum, E. H. Kong, J. Y. Son, Y. S. Kwon, T. Park and H. M. Jang, *J. Mater. Chem.*, 2011, **21**, 9582–9586.

28 F. Huang, D. Chen, X. L. Zhang, R. A. Caruso and Y.-B. Cheng, *Adv. Funct. Mater.*, 2010, **20**, 1301–1305.

29 S. Dadgostar, F. Tajabadi and N. Taghavinia, *ACS Appl. Mater. Interfaces*, 2012, **4**, 2964–2968.

30 X. H. Sun, Y. M. Liu, Q. D. Tai, B. L. Chen, T. Peng, N. Huang, S. Xu, T. Y. Peng and X. Z. Zhao, *J. Phys. Chem. C*, 2012, **116**, 11859–11866.

31 D. Chen, L. Cao, F. Huang, P. Imperia, Y.-B. Cheng and R. A. Caruso, *J. Am. Chem. Soc.*, 2010, **132**, 4438–4444.

32 D. Chen, F. Huang, L. Cao, Y.-B. Cheng and R. A. Caruso, *Chem.–Eur. J.*, 2012, **18**, 13762–13769.

33 W. E. Vargas and G. A. Niklasson, *J. Opt. Soc. Am. A*, 1997, **14**, 2243–2252.

34 G. Schlichthörl, N. G. Park and A. J. Frank, *J. Phys. Chem. B*, 1999, **103**, 782–791.

35 J. Krüger, R. Plass, M. Grätzel, P. J. Cameron and L. M. Peter, *J. Phys. Chem. B*, 2003, **107**, 7536–7539.

36 K. Zhu, N. R. Neale, A. Miedaner and A. J. Frank, *Nano Lett.*, 2007, **7**, 69–74.